24th Australasian Fluid Mechanics Conference - AFMC2024
Canberra, Australia
1-5 December 2024

Paper No: AFMC2024-72
DOI:10.5281/zenodo.14213445

The Influence of a Retro-Propulsion Plume on Vehicle Aerodynamics and Aeroheating during Hypersonic Re-Entry

Reuben Rankin[1*], **Tamás Bykerk**[2]

[1] The University of Newcastle, School of Engineering, Newcastle, 2308, Australia
[2] The German Aerospace Center, Bunsenstr. 10, Göttingen, 37073, Germany
*Email: reubenrankin@hotmail.com

Abstract

This paper investigates the aerodynamic and aeroheating effects on a re-usable launch vehicle during hypersonic re-entry, focusing on the transition from high-altitude glide to powered descent. Using the RFZ model, an open-source research geometry for reusable launch vehicles, the numerical analysis revealed significant influence of the plume on aerodynamic coefficients and surface heating. Plume-on and plume-off scenarios were tested at two angles of attack (0° and 9°). The plume-off cases showed that drag was predominantly attributed to high pressure on the baseplate and nozzle surfaces. This is in agreement with results from literature for a cylinder immersed in an axial flow. The plume-on cases demonstrated that plume shielding reduced total axial force coefficient, and significantly decreased heat transfer to the baseplate. Future work will look to investigate other trajectory points during powered descent, as well as supplementary angles of attack.

1 Introduction

Aeronautical engineers have a long history of developing standardised models for wind tunnel calibrations and data comparisons between facilities. They are useful in providing datasets for correlation of results, data repeatability over time and verifying model installation or data acquisition systems. Reference models are also relevant from the perspective of numerical analysis; different codes can be directly compared or assumptions and solver settings can be experimented with to determine solution sensitivity to certain parameters. A standardised reference model typically fulfills two main criteria. Firstly, they are simplistic in shape with a precisely defined geometry and secondly, they are representative of realistic configurations to ensure that the results are relevant. Examples of historical standard models include the AGARD-B (North Atlantic Treaty Organization, 1958), ONERA-M (Galway and Mokry, 1977) and the Standard Dynamics Model (SDM) (Beyers and Huang, 1990), while models such as the NASA CRM (Rivers et al., 2015) and the SSAM-Gen5 (Giannelis et al., 2023) provide more contemporary and relevant aircraft geometries from the past two decades.

Until recently, there has been no reference model for the space community. The RFZ model was developed in response to the sudden and urgent interest in re-usable spacecraft over the past decade (Bykerk, 2023). It serves as a standard test case for the research community to facilitate validation of numerical techniques in the generation of aerodynamic and aerothermal data over an entire trajectory. Since its introduction, work has been conducted on both the first (Karl et al., 2024) and second stage geometries (Basov et al., 2024; Ertl and Bykerk, 2024), with all results made available for public use (Bykerk, 2024).

This paper considers the RFZ model and focuses on the transition phase from high-altitude glide (plume-off) to powered descent (plume-on), which occurs at an altitude of approximately 58km and a Mach number of 7.14. An introduction to the geometry of the RFZ model will be given first. This is followed by an overview of the trajectory and the considered test matrix. Next, the numerical setup used for the Computational Fluid Dynamics (CFD) simulations is outlined, before the results are presented and discussed. Finally, a summary of results and potential avenues for future work is given.

2 RFZ Model

The RFZ model is based on the SpaceX Falcon 9, with the launch, entry and landing configurations presented in Figure 1 below. A comprehensive overview of the design is available in Bykerk (2023), while each of these geometries, as well as the second stage, are available for download in Bykerk (2024). This paper is concerned with the re-entry configuration, which is characterised by extended planar fins, retracted landing legs, and the lack of second stage (RFZ-REC).

Copyright is held by the author(s) through the Creative Commons BY-NC 4.0 License

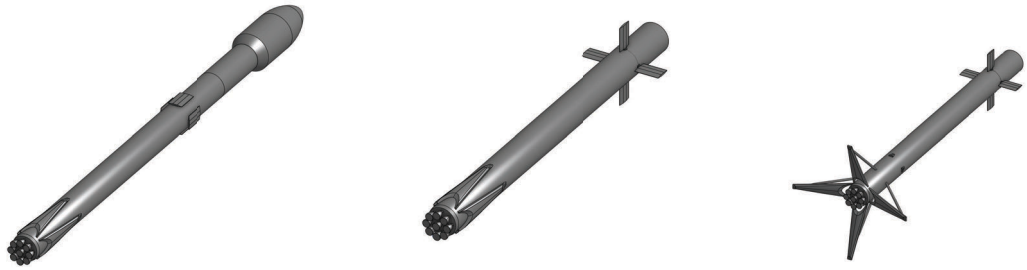

(a) Launch configuration (RFZ-LAC). **(b)** Re-entry configuration (RFZ-REC). **(c)** Landing configuration (RFZ-LDC).

Figure 1. Images showing different views of the RFZ model in various flight configurations.

3 Vehicle Trajectory and Point of Interest

Re-usable launchers of this type typically follow one of two different trajectory types. The first is a downrange landing, where the first stage is left to follow a natural arc after stage separation and lands away from the launch site. The second is a return to landing site scenario, where following stage separation the first stage alters its trajectory by performing a boost back burn to allow it to land at a designated landing zone close to the launchpad. For both cases the vehicle will complete a re-entry burn, an aerodynamic glide and finally a landing burn. Note that during these phases of flight, the vehicle is flying backwards. The work presented in this paper focuses on a downrange landing scenario, with an overview of the trajectory given below in Figure 2 for a low earth orbit (LEO) flight (Bykerk, 2023).

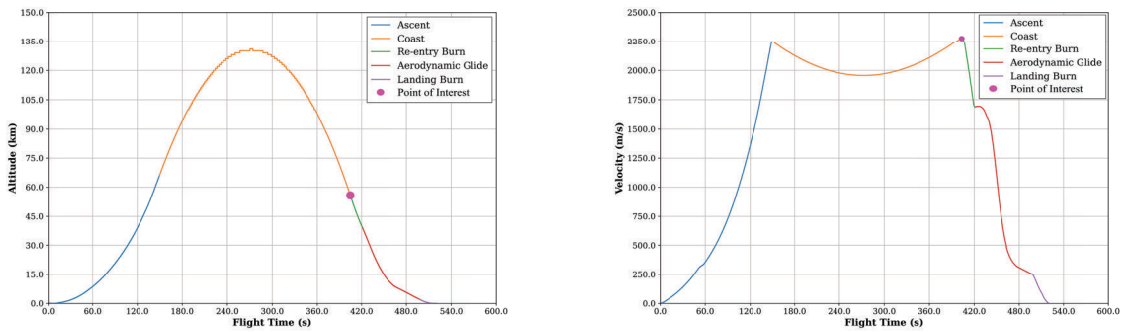

(a) Altitude **(b)** Velocity

Figure 2. LEO trajectory for the first stage with key events.

After an initial ascent burn of 149 seconds, stage separation occurs and the engines are shut-down. Once the second stage engine has been ignited and continues its journey to orbit, the booster performs a flip manoeuvre, before entering its coast phase. The vehicle reaches apogee during this phase at 272 seconds, after which the vehicle begins descending rapidly as seen in Figure 2 (a). The point of interest (POI) for this study occurs at the transition from the coast phase to the re-entry burn phase at 403 seconds, where three of the nine engines are fired to rapidly decelerate the spacecraft, as denoted by the pink dot in Figure 2. The vehicle is exposed to a freestream Mach number of 7.14 at an altitude of approximately 58km in the snapshot both before and after the engines are fired. There are no active control surface deflections considered during this time. To understand the sensitivity of the flowfield to Angle of Attack (AoA), as well as identify variations in heating patterns on the external surfaces of the vehicle, simulations have been conducted at 0° and 9°. The AoA variation alongside the plume-on and plume-off scenarios results in a total of four test cases, which are summarised in Table 1.

Altitude (km)	V_∞ (m/s)	P_∞ (Pa)	T_∞ (K)	AoA (deg)	Plume (on/off)	Mach No. (-)
57.66	2281.9	30.02	253.3	0	off	7.14
57.66	2281.9	30.02	253.3	0	on	7.14
57.66	2281.9	30.02	253.3	9	off	7.14
57.66	2281.9	30.02	253.3	9	on	7.14

Table 1. Test matrix denoting operating conditions for each test case.

4 Numerical Setup

The TAU code is a second order finite-volume solver for the Euler and Navier-Stokes equations which includes a comprehensive range of RANS-based or scale resolving turbulence models. It uses unstructured computational grids to facilitate the analysis of complex geometries and is highly optimised for the application on massively parallel High Performance Computing (HPC) systems. TAU has been successfully applied to a wide range of sub-to-hypersonic flow problems, both in scientific and industrial applications, including the analysis of re-usable launcher configurations (Ecker, 2020; Bykerk et.al., 2020; Bykerk, 2022, 2023). The calculation of the inviscid fluxes in the finite volume framework is based on the application of the AUSMDV flux vector splitting scheme together with MUSCL gradient reconstruction to achieve second order spatial accuracy. Viscous fluxes are treated with a low-dissipation central discretisation scheme.

Turbulence was modelled with the k-ω-SST Model from Menter. An adequate setup of the numerical grid is required which is achieved by using prismatic sub-layers close to the wall with a first dimensionless wall spacing of y^+ in the order of one and a wall normal stretching ratio of grid cells of less than 1.3. An isothermal wall temperature of 300 K was used which allows for conservative heat flux estimations. A spherical domain with approximately 50 rocket lengths upstream and downstream of the vehicle centrepoint has been used. Two separate but similar meshes were used for the plume-on and plume-off cases. Within each mesh, refinement blocks have been placed around the entire vehicle, as well as around the base region, which can be seen in Figure 3. For the AoA = 0° cases, a quarter grid was used to exploit the vehicle flow symmetry, reducing computational expense. For the AoA = 9° cases, the grid was mirrored about the x-y plane and fused to form a half grid. Mesh generation was conducted using CENTAUR. Refinement blocks for the plume-off case can be seen in Figure 3 (a), while Figure 3 (b) shows the plume-on case grid. The various grid refinement sources have been sized based on preliminary studies not presented in this paper, where critical features of the flow topology were identified. Examples of this include bow shock location, degree of radial plume spreading as well as the plume penetration length.

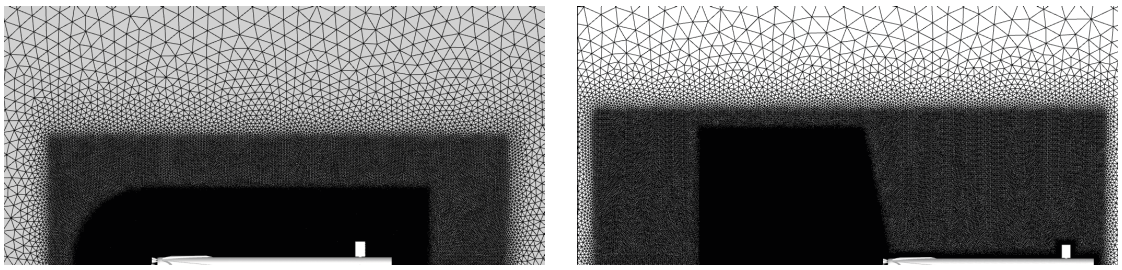

(a) Plume-Off Mesh Overview. **(b)** Plume-On Mesh Overview.

Figure 3. Overview of RANS grid.

Figure 4 (a) shows the separate wall boundaries for the evaluation of component contributions to global force coefficients. The red surfaces denote the fins, the wall is coloured yellow, the nozzles are denoted by blue, the baseplate shown in pink and the landing legs in grey. The interstage is typically a small cavity which extends internally down to the fins. For these investigations, the interstage bay has been sealed and is shown in green. For all cases, the nozzle exits have been sealed. For plume-on simulations, dirichlet boundary conditions have been assigned to the exit planes of the three active engines, as seen in red in Figure 4 (b). This allows user defined setting of all values at the boundary, which is critical for accurately representing the outflow properties of the nozzle. Examples of these include as axial and radial components of velocity, as well as density and pressure. These have been quantified during separate 2D axisymmetric simulations (Bykerk, 2023). The farfield, which has not been shown, is an inflow/outflow boundary far away from the investigated configuration for external flow. All gradients are assumed to be zero and therefore no viscous effects are taken into account.

For the plume-off cases, the air was treated as a perfect gas. For plume-on cases, this assumption cannot be applied to the high temperature exhaust gases. CFD simulations for these cases are based on a two species approach, where atmospheric air and nozzle exhaust are separate gas mixtures with their own thermodynamic and transport properties. Both atmospheric air and nozzle exhaust species are considered chemically frozen and thermally perfect. The atmospheric air is composed of 77% N_2 and 23% O_2 by mass fraction, while the mass fractions for the nozzle exhaust, namely CO (37.4%), CO_2 (35.5%), H_2 (1.2%), H_2O (25.9%), are taken from previous work considering kerosene and liquid oxygen, with an oxidiser-to-fuel ratio of 2.35 (Bykerk, 2023). The tabulated thermodynamic and transport properties of the air and exhaust species required for the TAU computations are calculated using an in-house tool which applies the data contained within the NASA

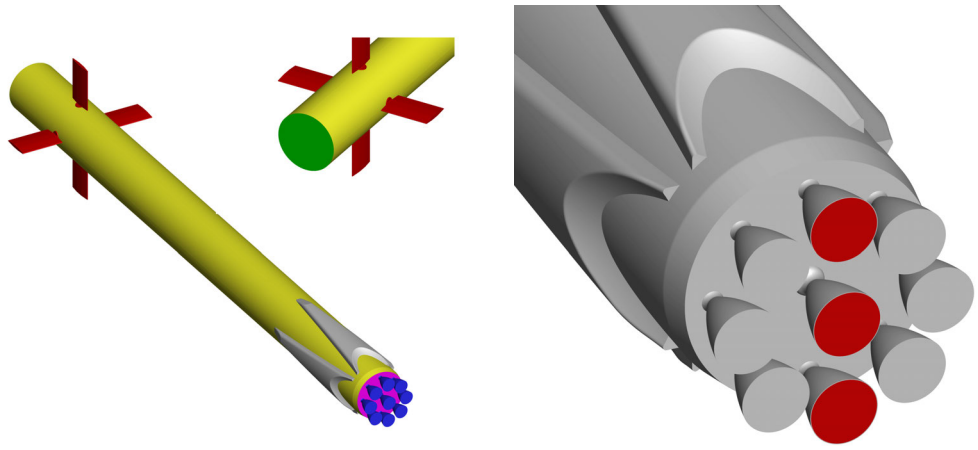

(a) Wall boundaries for force reporting **(b)** Active nozzles with Dirichlet boundary condition

Figure 4. Overview of boundary conditions used for

CEA databases (Gordon, 1994) as well as the Wilke rule. During the CFD runs, where exhaust and air species interact, the Wilke rule is also used to calculate the transport properties of the air-exhaust mixture, which is dependent on the gas composition, i.e. mass fractions of air and exhaust, as well as the pressure and density. The two frozen species modelling approach removes the computational expense associated with the use of chemical kinetic mechanisms, but also has limitations, such as the inability to capture post combustion (Laureti, 2024). Nevertheless, these results can form the basis of future work looking the quantify the effects of chemistry modelling on the aerodynamic characteristics of the vehicle as well as surface heat fluxes.

5 Grid Convergence Study

Conducting a grid convergence study was a critical aspect of the investigation to ensure that the numerical solutions were independent of mesh resolution. Grid convergence studies can also help realise the balance between computational cost and the gained accuracy associated with finer meshes. Three levels of grid refinement were considered: coarse, medium, and fine, with point counts of 2.3 million, 11 million, and 77 million, respectively. These counts were reached via halving the length scale for the refinement regions between each mesh density. The grid convergence study was conducted for the plume-on case only. The criteria used for the grid convergence study was the surface heat flux integral as well as the global axial force coefficient (C_{Fx}). The resulting heat flux and axial force coefficient computed for the three grids are summarised in Table 2. The medium mesh was selected due to the small differences (less than 1%) observed for both heat flux and C_{Fx} between the medium and fine grid results.

Grid Level	**Heat Flux (W/m^2)**	**% Diff. (Heat Flux)**	C_{Fx}	**% Diff. (C_{Fx})**
Coarse	1.2761×10^6	-	0.554	-
Medium	1.2844×10^6	0.65	0.580	4.48
Fine	1.2850×10^6	0.05	0.582	0.34

Table 2. Convergence criteria across different grid levels.

6 Results

6.1 Plume-Off Flow and Aerothermal Heating Analysis

Figure 5 presents the Mach number field and base plate convective heat flux contours for both plume-off AoA cases. The global flow field is shown in Figures 5 (a) and 5 (d), while a close-up of the base region can be seen more clearly in Figures 5 (b) and 5 (e). Here it can be observed that the freestream Mach 7.14 flow passes through a strong bow shock and decelerates rapidly. For both AoA cases, the standoff distance of the bow shock is quite small, and in the case of AoA = 9°, skewed via the angled oncoming flow. As a result, the

windward nozzles experience a smaller shock standoff distance. The influence of AoA on the flowfield can be easily identified visually, where the 0 AoA case has a uniform Mach number of approximately 3 around the vehicle, while at 9 degrees AoA the Mach 3 region is largely confined to the leeward side. This also causes strong variations in heating downstream, particularly on the fins. Fin 3 on the windward side sees the highest heating as it is exposed to the higher energy freestream, while leeward Fin 1 is shielded, experiencing the lowest amount of heating (see Figure 5 (d)).

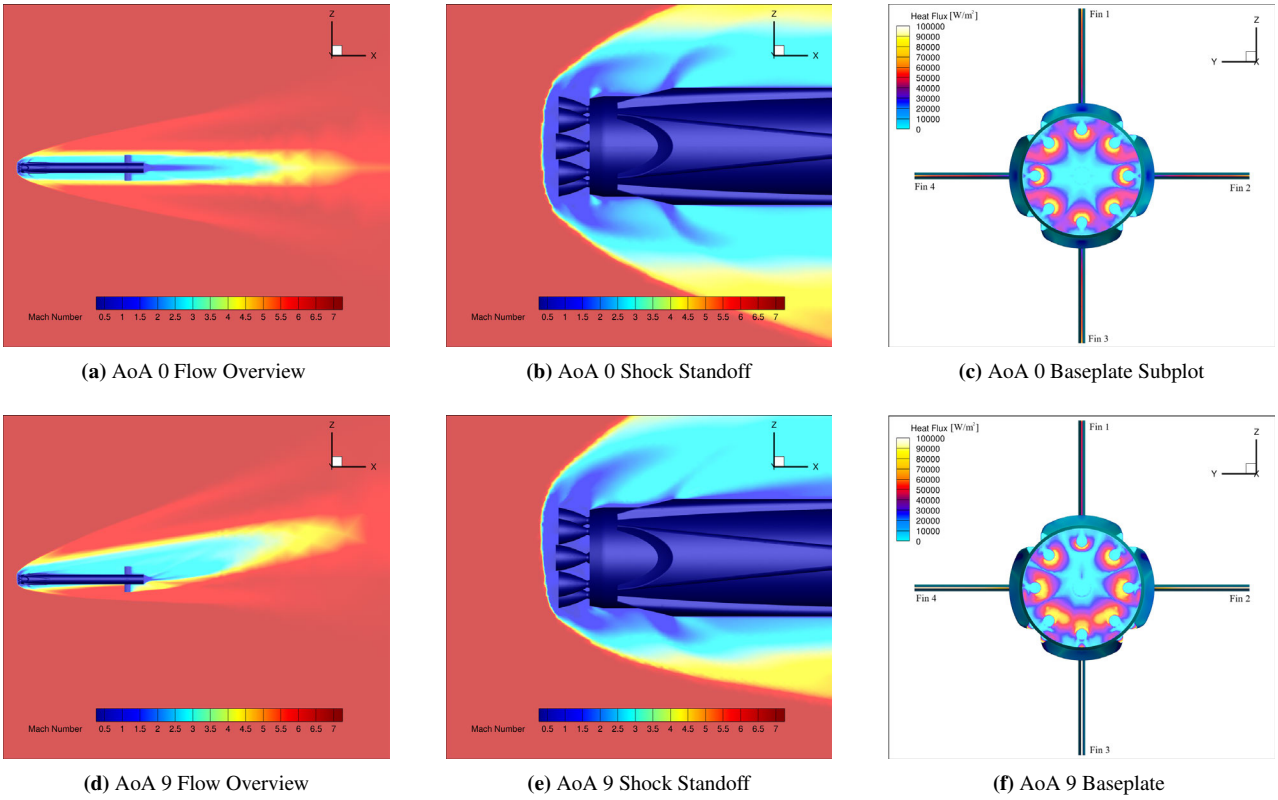

(a) AoA 0 Flow Overview **(b)** AoA 0 Shock Standoff **(c)** AoA 0 Baseplate Subplot

(d) AoA 9 Flow Overview **(e)** AoA 9 Shock Standoff **(f)** AoA 9 Baseplate

Figure 5. Plume-off Mach number contour and baseplate heat flux contour for both AoA cases

Convective heat flux on the baseplate for both cases is displayed in Figures 5 (c) and 5 (f). Regions of high heat flux correspond to areas where the flow is stagnated, while regions of lower heatflux are associated with flow separation and recirculation regions. Note that the heat flux is largely symmetric for the 0 degree AoA case as seen in Figure 5 (c). Some slight variances in heat flux are observed at the z-normal symmetry plane which requires further investigation. In the case of AoA = 9°, asymmetry in the baseplate heat flux contours about the y-axis is directly caused by the increased level of stagnation on the bottom portion of the baseplate (where the oncoming flow originates), while on the top half of the baseplate lower heatfluxes are observed, particularly due to the augmented wake of the central nozzle.

6.2 Plume-On Flow and Aerothermal Heating Analysis

Large plume expansion due to high altitude operating conditions can be seen in both Figures 6 (a) and 6 (c). The high degree of spreading is a typical characteristic of an under-expanded plume, and is the result of a low freestream static pressure compared to the exit pressure of the nozzle. Observed in Figure 6 (a), the bow shock is pushed downstream of the active engines. Behind the bow shock the streamlines coalesce and form a contact surface downstream of the Mach disk from the plume, resulting in a free stagation point. The shape of the plume is characterised by a longer penetration of the central engine exhaust, due to the presence of high velocity exhaust gases from the peripheral nozzles preventing significant flow expansion and directing the flow momentum axially. On the contrary, the outer nozzles expand freely in the radial direction, causing a shorter penetration length. As a result, the plume appears to have ramps either side of the Mach disk. In addition to the flow separation observed at these locations, a large wake can also be seen on the leeward side of the plume.

In contrast to the AoA = 0°, Figure 6 (c) shows an asymmetric plume due to the angled freestream. This alters the recirculation region sizes and locations compared to the baseline case. On the leeward side of the vehicle, larger areas of separated flow are observed, while on the windward side a small recirculation zone is

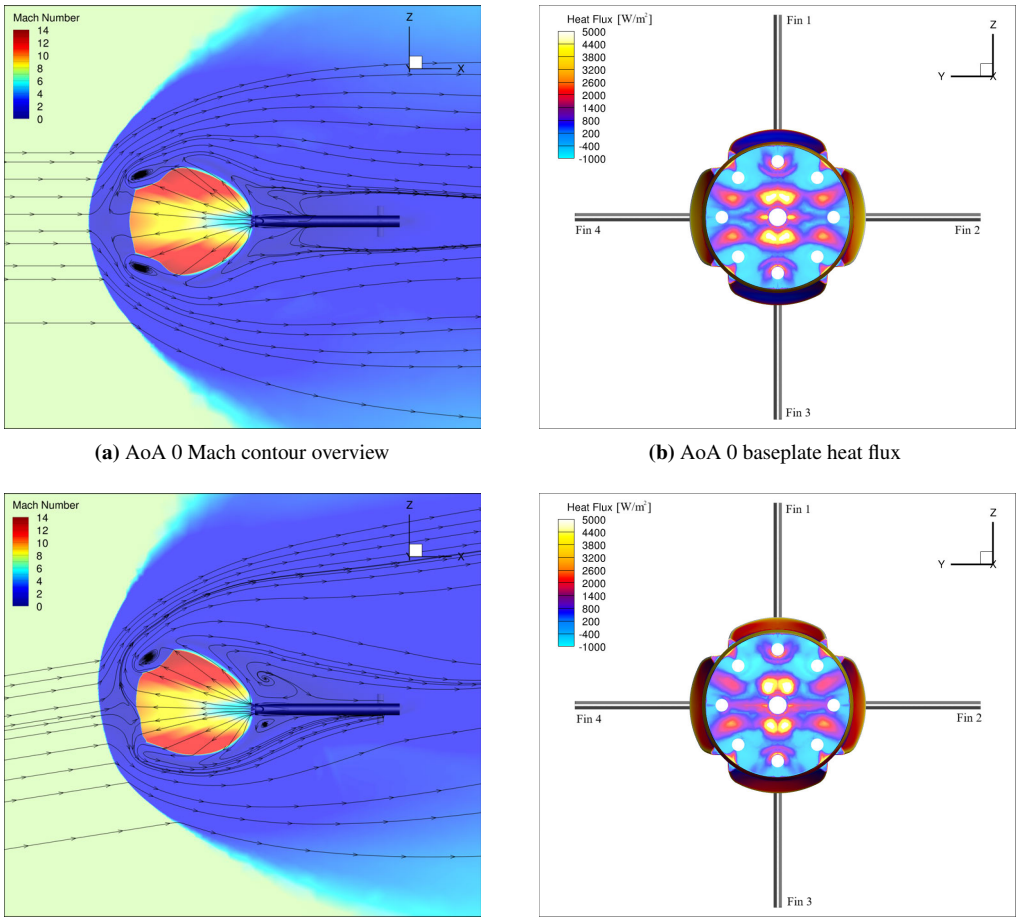

(a) AoA 0 Mach contour overview

(b) AoA 0 baseplate heat flux

(c) AoA 9 Mach contour overview

(d) AoA 9 baseplate heat flux

Figure 6. Plume-on Flowfield and baseplate heat flux for AoA = 0° and AoA = 9° cases.

visible. The shifted plume allows the flow to reattach to the surface of the vehicle on the windward side, which was not seen in the 0 degrees AoA case. Close to the baseplate, the flow is dominated by plume interaction effects and as a result, only a small influence of AoA is seen in this region. This is reflected when comparing the heat flux patterns in Figure 6 (b) and 6 (d). It can be seen that the heat flux patterns remain largely similar despite the change in AoA. Local maxima of 5 kW/m^2 can be found around the central active engine in Figures 6 (b) and 6 (d). It is important to note that the heat flux on the baseplate is an order of magnitude lower than the results produced by the plume-off cases, and much lower than the heat flux experienced by the fins. These results are consistent with the phenomena of plume shielding, whereby the overall plume structure shields the exterior surfaces from the hypersonic freestream, significantly reducing convective heat.

6.3 Comparison of Axial Force Between Plume-On and Plume-Off

Table 3 presents a breakdown of the axial force coefficient as per the defined wall boundaries which are visualised in the bar graphs in Figure 7.

Case	Baseplate	Wall	Nozzles	Interstage	Legs	Fins	Total
Plume-off AoA 0	0.758	0.044	0.754	0.018	0.042	0.028	**1.644**
Plume-off AoA 9	0.748	0.058	0.733	0.024	0.044	0.077	**1.684**
Plume-on AoA 0	0.266	0.019	0.326	-0.039	-0.005	0.013	**0.580**
Plume-on AoA 9	0.266	0.039	0.326	-0.022	-0.006	0.036	**0.639**

Table 3. X-force coefficient breakdown by region in each sub-case

Naming conventions for the legs follow the same style as the fins, as labeled in the previous baseplate heat flux Figures. Individual contributions of legs and fins can be seen in Figure 7 and have been added together respectively within Table 3.

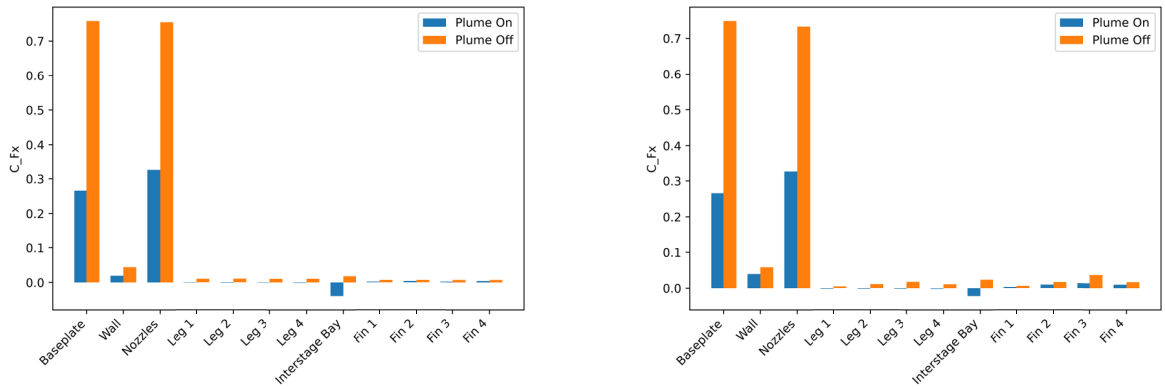

(a) AoA 0

(b) AoA 9

Figure 7. C_{Fx} bar graph comparison Plume-on VS Plume-Off

As expected, plume-off cases show much higher C_{Fx} values than plume-on cases, largely due to the plume shielding that occurs in the plume-on cases which dramatically reduces the pressure acting on the base region. Comparing the no plume cases for AoA = 9° with AoA = 0°, it can be seen that the axial force does not change significantly, as the base region of the rocket is still heavily exposed to the oncoming flow. This also holds true for the plume-on case, where contributions remain similar. As discussed previously, the AoA is only seen to influence the global flowfield, rather than the base area nearfield. The largest fin forces are seen on fin 3, which is more exposed to the freestream in the case of AoA = 9° compared to AoA = 0°. In addition, forces acting on the wall boundary due to viscous effects are higher with the plume-off. While no experimental validation for either of these cases is available, a basic comparison between a cylinder exposed to an axial flow in ref. Hoerner (1965) can be made. Here it is highlighted that the nose pressure contributes to around 90% of the total axial force coefficient at Mach 7, which agrees well with these findings. In addition, the reported coefficient for a cylinder is approximately 1.7, which aligns closely to the calculated 1.65 in this work.

7 Conclusions and Future Work

This paper has examined the effects of vehicle aerodynamics and aeroheating during hypersonic re-entry; specifically, during the transition from high-altitude glide to powered descent. The results generated within this investigation used the RFZ model; an open-source, common research geometry for reusable launch vehicles. The analysis has revealed that the plume significantly influences aerodynamic coefficients and surface heat flux characteristics. Distinct variations were observed between plume-on and plume-off scenarios, which were both tested at an AoA of 0° and 9°.

Simulation results for the plume-off case at AoA = 0° is in good agreement with published results for a simple cylinder placed in an axial hypersonic flow. Without the presence of a plume, the global axial force coefficient is dominated by the high pressure on the baseplate and nozzle surfaces. With the presence of the plume, the axial force associated with the base area reduces dramatically. The solutions showed no sensitivity to AoA in terms of base heating patterns and forces. This is because the AoA was only seen to affect the flowfield downstream of the nozzles and as a result, mainly altered the flowfield around the body of the rocket. The work conducted in this paper makes the first powered descent results available to the RFZ rocket research community, providing the first openly available numerical test case for re-usable launchers utilising a retro-propulsion descent strategy.

Future work will look to evaluate other trajectory points during the re-entry and landing burns, as well as investigate further AoA variations. Additionally, experimental validation through wind tunnel tests would be invaluable in corroborating the numerical findings and refining computational models.

References

Galway, R.D. and Mokry, M., 1977, Wind Tunnel Tests of ONERA Aircraft Models, National Aeronautical Establishment.

North Atlantic Treaty Organization. Advisory Group for Aeronautical Research and Development, 1958, Wind Tunnel Calibration Models - AGARD Specification 2, NATO.

Beyers, M. and Huang, X., 1990, Subsonic Aerodynamic Coefficients of the SDM at Angles of Attack up to 90°, NRC, Ottowa, Canada.

Rivers, M. B., Quest, J., and Rudnik, R., 2015, Comparison of the NASA Common Research Model European Transonic Wind Tunnel Test Data to NASA Test Data (Invited), AIAA SciTech Forum, Florida, January.

Giannelis, N.F., Bykerk, T., and Vio, G.A., 2023, A Generic Model for Benchmark Aerodynamic Analysis of Fifth-Generation High-Performance Aircraft, Aerospace, 10(9), Article 746. URL: https://www.mdpi.com/2226-4310/10/9/746, ISSN: 2226-4310.

Basov, L., Ertl, M., and Bykerk, T., 2024, Comparison of Fokker-Planck and CFD simulations of the RFZ-ST2 upper stage, HiSST: 3rd Int. Conference on High Speed Vehicle Science, Busan, Korea, April.

Ertl, M., and Bykerk, T., 2024, A standard model for the investigation of aerodynamic and aerothermal loads on a re-usable launch vehicle - second stage geometry, HiSST: 3rd Int. Conference on High Speed Vehicle Science and Technology, Busan, Korea, April.

Karl, S., Bykerk, T., and Laureti, M., 2024, Design of a truncated ideal nozzle for a re-usable first stage launcher, HiSST: 3rd Int. Conference on High Speed Vehicle Science, Busan, Korea, April.

Bykerk, T., 2023, RFZ Data Repository, URL: https://zenodo.org/records/8146567.

Bykerk, T., 2023, A standard model for the investigation of aerodynamic and aerothermal loads on a re-usable launch vehicle, 10th EUCASS – 9th CEAS Conference 2023, Lausanne, Switzerland, July.

Ecker, T., Karl, S., Dumont, E., Stappert, S., Krause, D., 2020, "Numerical Study on the Thermal Loads During a Supersonic Rocket Retropropulsion Maneuver," Journal of Spacecraft and Rockets, Vol. 57, No. 1.

Bykerk, T., Karl, S., 2023, "Preparatory CFD Studies for Subsonic Analyses of a Reusable First Stage Launcher during Landing within the RETPRO Project," Int. Conference on Flight Vehicles, 9th European Conference for Aeronautics and Space Sciences (EUCASS), Lausanne, Switzerland, July.

Bykerk, T., Kirchheck, D., Karl, S., 2022, "Reconstruction of Wind Tunnel Tests using CFD for a Reusable First Stage during Rocket Retro-Propulsion" Int. Conference on Flight Vehicles, 9th European Conference for Aeronautics and Space Sciences (EUCASS), Lille, France, July.

Bykerk, T., Kirchheck, D., Karl, S., 2022, "Condensation Modelling of Expanding Cold Gas Jets during Hypersonic Retro-Propulsion Manoeuvres within the RETPRO Project," 23rd Australasian Fluid Mechanics Conference (AFMC), Sydney, Australia, December.

Bykerk, T., Kirchheck, D., Karl, S., 2022, "Condensation Modelling of Expanding Cold Gas Jets during Hypersonic Retro-Propulsion Manoeuvres within the RETPRO Project," 23rd Australasian Fluid Mechanics Conference (AFMC), Sydney, Australia, December.

Hoerner, S.F., 1965, *Fluid Dynamic Drag: Practical Information on Aerodynamic Drag and Hydrodynamic Resistance*.

Gordon, S., McBride, B. J., 1994, "Computer Program for Calculation of Complex Chemical Equilibrium Compositions and Applications," NASA Reference Publication, 1311.

Laureti, M., Karl, S., Bykerk, T., Kirchheck, D., 2024, "Aerothermal Analysis of the RETPRO Flight Configuration," 9th Edition of the Int. Conference on Space Propulsion 2024, Glasgow, Scotland, May, pp. 1-11.